J Adv Ceram

Research Article

Reviving the activity of Si-contaminated cathodes via chloride anion doping for proton-conducting solid oxide fuel cells

Wenhui Song, Xianchen Dong, Yanru Yin, Shoufu Yu, Yueyuan Gu✉, Lei Bi

Cite this article: Song W, Dong X, Yin Y, et al. *J Adv Ceram* 2026, **15**(4): 9221262. https://doi.org/10.26599/JAC.2026.9221262

ABSTRACT: Silicon contaminants, often introduced from raw materials or sealants, severely impair the performance of perovskite cathodes in proton-conducting solid oxide fuel cells (H-SOFCs). To counteract this poisoning effect, this study proposes a chloride anion doping strategy to mitigate the detrimental impact of Si contamination, using $La_{0.5}Sr_{0.5}FeO_3$ (LSF) as a case study. While Si doping increases the oxygen vacancy formation energy and slows oxygen/proton transport in LSF, the co-incorporation of Cl^- effectively reverses these adverse changes. Cl doping expands the lattice, promotes charge redistribution, and significantly reduces the energy barrier for vacancy formation. These structural modifications enhance both bulk diffusion and surface exchange kinetics for oxygen and proton species, as confirmed by electrical conductivity relaxation measurements. More importantly, the Cl-Si codoping strategy not only offsets the negative effects of Si contamination but also improves material properties beyond those of contamination-free LSF. As a result, the Cl-doped cathode achieves a peak power density of 1537 mW·cm^{-2} at 700 °C, outperforming even the fuel cell with a pristine LSF cathode. Furthermore, the cell exhibits excellent operational stability. This work demonstrates that purposeful anion doping can effectively alleviate cation-impurity poisoning and offers a viable route toward developing cost-effective and durable cathodes for H-SOFCs.

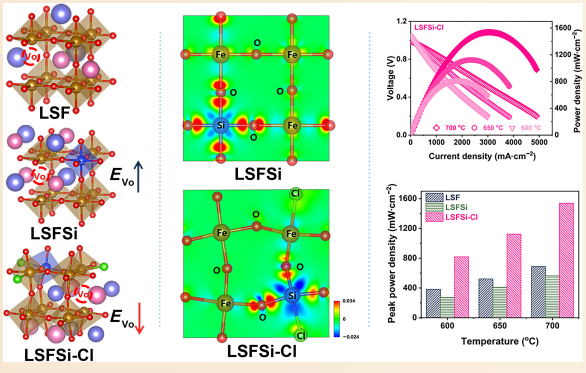

KEYWORDS: solid oxide fuel cells; proton conductor; cathode; anion doping

1 Introduction

During the global shift toward sustainable energy, solid oxide fuel cells (SOFCs) are considered a promising technology due to their excellent energy conversion efficiency [1,2]. Traditional SOFCs, which rely on oxygen-ion-conducting electrolytes, usually require high operating temperatures (800–1000 °C), which not only complicate sealing and durability but also restrict their practical application [3–5]. Although some oxygen-ion conductors, such as doped Bi_2O_3, show high conductivities at intermediate temperatures, the instability of Bi_2O_3 under low oxygen partial pressure conditions makes the direct exposure of doped Bi_2O_3 electrolyte to the anode environment challenging, and a blocking layer is usually needed [6]. In contrast, proton-conducting SOFCs (H-SOFCs) offer a compelling alternative because they use proton-conducting electrolytes, which have low activation barriers for proton migration [7–9]. Therefore, they can operate effectively at intermediate temperatures (400–700 °C) and solve the high-temperature working problem for traditional SOFCs [10–12]. Another intrinsic advantage of H-SOFCs is the formation of water on the cathode side, thereby preventing fuel dilution on the anode side and improving overall fuel utilization [13,14]. Because ceramic materials are used as the main components, H-SOFCs are also known as protonic ceramic fuel cells (PCFCs). Despite these benefits, the use of H-SOFCs is still hampered by the limited performance of cathode materials, as reduced operating temperatures dramatically slow the kinetics of the oxygen reduction reaction (ORR), making the development of cathodes with high ORR activity a critical target [15–18]. In addition, practical applications require long-term stability and resilience against impurity effects, which directly influence the viability and lifetime of H-SOFC systems [19–21].

In practical operating environments, the performance of cathode materials is often compromised by impurity contamination [22–24]. Among these, silicon is frequently introduced via raw materials or glass-based sealants, which is particularly detrimental, as it is known to induce insulating secondary phases and significantly degrade electrochemical kinetics [25,26]. Current mitigation strategies largely rely on high-purity materials, an approach that inevitably increases system costs and complicates large-scale deployment. Therefore, designing cathode materials capable of tolerating, or even

Fuel Cell Group, School of Resource Environment and Safety Engineering, University of South China, Hengyang 421001, China.

✉ Corresponding author. E-mail: guyueyuan@usc.edu.cn

Received: December 29, 2025; Revised: January 30, 2026; Accepted: February 8, 2026

functionally accommodating, trace silicon impurities represents a valuable direction, which could lower cost barriers and improve long-term operational stability for H-SOFCs.

While traditional approaches to improve cathode catalytic activity have largely relied on cation substitution [27–30], recent attention has shifted toward anion doping as a complementary strategy [31,32]. Among various anionic dopants, halogen elements (especially chloride) offer distinct potential [33]. Due to its lower electronegativity and larger ionic radius relative to oxide ions, partial substitution of oxygen with chloride in perovskite lattices can elongate metal–oxygen bonds and increase the crystallographic free volume. These structural and electronic adjustments may counterbalance charge disturbances and mitigate lattice strain. This possibility raises an interesting prospect: introducing Cl^- into a silicon-affected cathode could alleviate poisoning effects through tailored anion chemistry, possibly even harnessing Si–Cl interactions to unlock synergistic performance gains.

To address this hypothesis, we select $La_{0.5}Sr_{0.5}FeO_3$ (LSF), a well-studied perovskite cathode material in the SOFC family [34] whose functionality is closely tied to its defect chemistry [35], as a model system. A minor amount of Si is introduced at the Fe site to simulate the detrimental impact of silicon impurities arising from low-purity precursors or sealant leaching. Subsequently, chloride is doped at oxygen sites to create a codoped composition, aiming to recover the compromised properties. Combining density functional theory (DFT) calculations with experimental characterization, this work systematically examines how Si single-doping and Si–Cl codoping alter the crystal structure, oxygen vacancy formation, and ultimately the electrochemical performance of LSF, thereby clarifying the mechanistic role of anion regulation in mitigating cation impurity poisoning.

2 Materials and methods

$La_{0.5}Sr_{0.5}FeO_{3-\delta}$ (denoted LSF), $La_{0.5}Sr_{0.5}Fe_{0.95}Si_{0.05}O_{3-\delta}$ (LSFSi), and $La_{0.5}Sr_{0.5}Fe_{0.95}Si_{0.05}Cl_{0.1}O_{2.9-\delta}$ (LSFSi-Cl) powders were synthesized via a conventional solid-state reaction method [36]. Stoichiometric amounts of La_2O_3, $SrCO_3$, and Fe_2O_3 were used as precursors. For doping, SiO_2 and $FeCl_3$ were employed as the silicon and chloride sources, respectively. The raw powders were ball-milled for 24 h in ethanol to ensure homogeneity. After drying, the mixtures were calcined at 1200 °C for 6 h to obtain phase-pure powders. The crystal structure of the as-synthesized powders was examined by X-ray diffraction (XRD), and the lattice parameters were refined by Rietveld analysis using the GSAS package. High-resolution transmission electron microscopy (HR-TEM) was employed to observe atomic-scale lattice fringes and to verify the homogeneity of Si and Cl doping. X-ray photoelectron spectroscopy (XPS) was used to analyze the concentration of surface oxygen vacancies and confirm the successful incorporation of Cl and Si. To evaluate the oxygen and proton diffusion as well as surface exchange kinetics, dense bars were prepared and studied by electrical conductivity relaxation (ECR) measurements under various atmospheres.

For electrochemical performance evaluation, anode-supported single cells with a configuration of NiO-$BaCe_{0.7}Zr_{0.1}Y_{0.2}O_{3-\delta}$ (BCZY) anode| BCZY electrolyte| cathode were fabricated via a copressing and cosintering process. The half-cells (anode with electrolyte) were sintered at 1350 °C for 6 h to densify the BCZY electrolyte membrane. The cathode slurries (LSF, LSFSi, and LSFSI-Cl) were then painted onto the electrolyte surface and fired at 900 °C to form complete cells. The fuel cells were tested under operating conditions using humidified H_2 as the fuel and static air as the oxidant. The electrochemical performance was assessed and compared using an electrochemistry workstation. The microstructure of the fuel cells was examined by scanning electron microscopy (SEM).

First-principles calculations were performed based on DFT using the Vienna *ab initio* simulation package (VASP) [37]. The projector-augmented wave (PAW) method was used to describe the ion-electron interactions [38]. The generalized gradient approximation (GGA) [39] with the Perdew Bruke–Ernzerhof (PBE) functional was employed for the exchange-correlation energy [40]. To better describe the strongly correlated 3d electrons of Fe, a Hubbard U correction (U_{eff} = 3.9 eV) was applied. A plane-wave cutoff energy of 520 eV was used, and the convergence criteria for energy and force were set to 10^{-5} eV and 0.05 eV·Å^{-1}, respectively.

3 Results and discussion

The phase purity and structural evolution of the synthesized LSF, LSFSi, and LSFSi-Cl cathodes were first examined by XRD. A high Sr-doping concentration was used for the LSF material due to the consideration of charge compensation. In the Sr-doped $LaFeO_3$ material, the La cation is 3+ and the Sr cation is 2+. By partially replacing La with Sr, extra oxygen vacancies are created, which might improve the activity of the cathode. Figure 1(a) presents the XRD patterns, where all samples exhibit sharp, characteristic perovskite peaks without detectable secondary phases. A discernible shift in peak positions is observed in both doped samples, indicating changes in lattice parameters due to the incorporation of Si and Cl. Further chemical state analysis via XPS confirms successful dopant integration. As shown in Fig. 1(b), in the Si 2p spectrum of LSFSi, the peak appears near 102.0 eV, which is distinct from that of typical SiO_2 (approximately 103.5 eV), suggesting that Si substitutes for Fe within the perovskite lattice rather than forming an insulating silica phase. Because of the ionic mismatch between Si and La and Sr, Si is unlikely to occupy the La or Sr site in LSF. Attempts have been made to prepare $La_{0.5}Sr_{0.45}Si_{0.05}FeO_{3-\delta}$ and $La_{0.45}Si_{0.05}Sr_{0.5}FeO_{3-\delta}$, and no pure phase materials can be obtained (Fig. S1 in the Electronic Supplementary Material (ESM)). For the codoped LSFSi-Cl, the Si 2p peak remains at a similar binding energy (~102.3 eV), while the Cl 2p spectrum displays the characteristic doublet, consistent with Cl^- incorporation into the oxygen sublattice. These findings are corroborated by TEM-EDS elemental mapping. Figure 1(c) reveals a homogeneous distribution of La, Sr, Fe, O, Si, and Cl in the LSFSi-Cl particles, with no evidence of localized segregation or secondary phase formation. Collectively, the XRD, XPS, and TEM-EDS results confirm the phase-pure nature of the materials and the effective lattice integration of both dopants. The material was synthesized by the solid-state reaction method, a straightforward approach with practical potential, while the homogeneity of the resulting powders in large-scale production needs further investigation.

Rietveld refinement of the XRD was conducted to quantify the structural modifications induced by doping (Fig. 2(a)). The R_p values for LSF, LSFSi, and LSFSi-Cl are 4.09%, 3.76%, and 4.56%, and the R_{wp} values are 5.23%, 4.82%, and 5.92%, respectively. For pristine LSF, the refined lattice parameter is $a = b = c = 3.92$ Å. Doping with Si reduces this value to 3.90 Å in LSFSi, a contraction consistent with the smaller ionic radius of Si^{4+} compared to $Fe^{3+/4+}$, which introduces compressive strain into the perovskite lattice. Introducing Cl alongside Si, however, produces a distinct effect, and the lattice parameter of LSFSi-Cl expands to 3.94 Å. This expansion can be attributed to the larger ionic radius of Cl^- relative to O^{2-}, which compensates for the Si-induced contraction

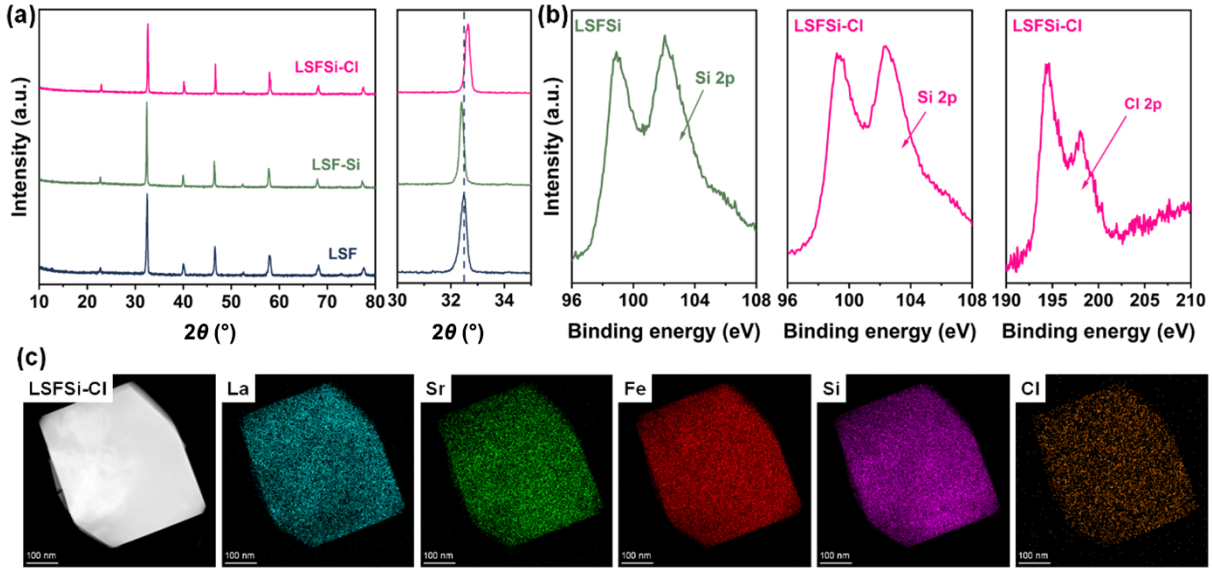

Fig. 1 (a) XRD patterns of LSF, LSFSi, and LSFSi-Cl. (b) XPS Si 2p spectra of LSFSi and LSFSi-Cl and Cl 2p spectra of LSFSi-Cl. (c) Elemental mappings of LSFSi-Cl.

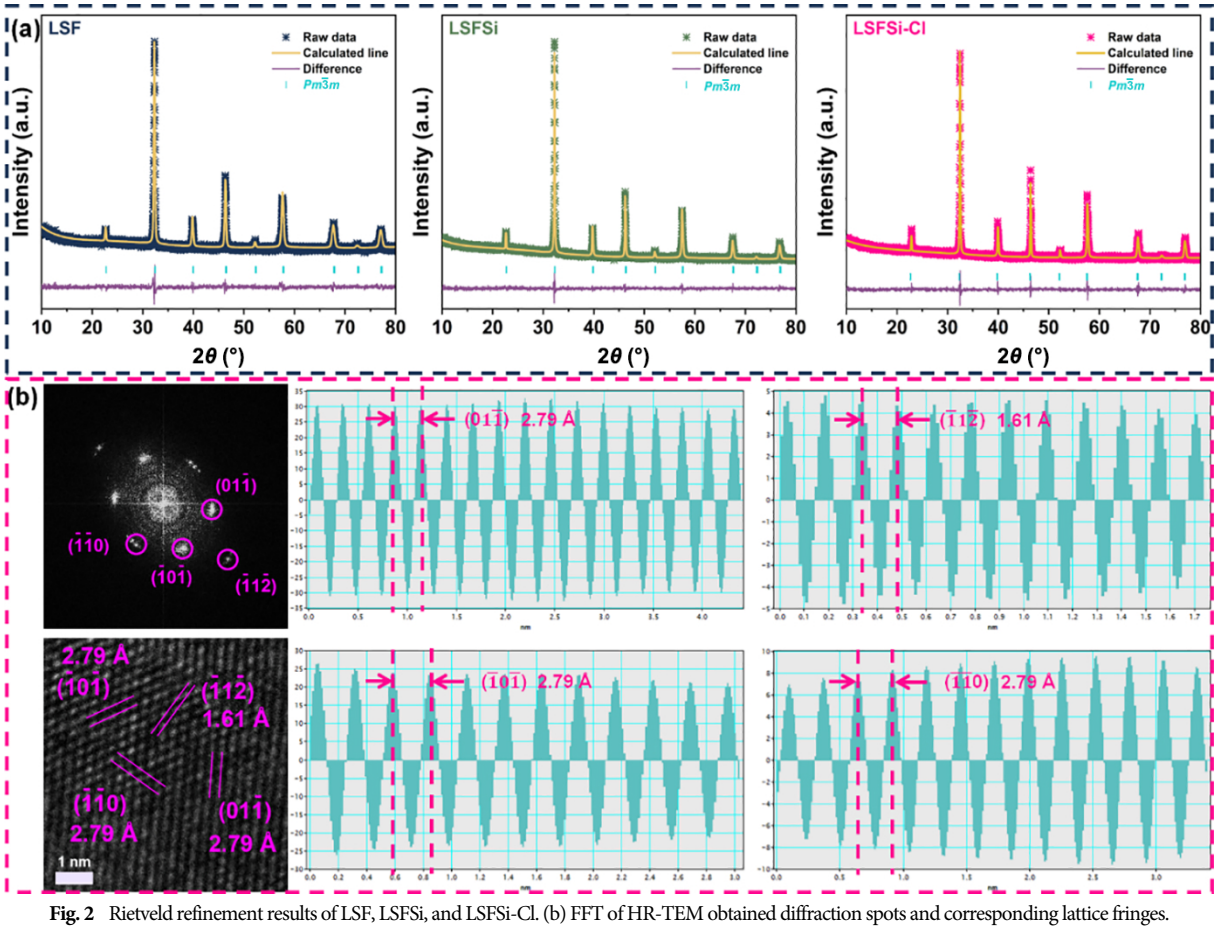

Fig. 2 Rietveld refinement results of LSF, LSFSi, and LSFSi-Cl. (b) FFT of HR-TEM obtained diffraction spots and corresponding lattice fringes.

and increases the crystallographic free volume. These trends align well with the observed peak shifts in the XRD patterns. The refinement goodness of fit-parameters (χ^2 = 1.22, 0.93, and 1.04 for LSF, LSFSi, and LSFSi-Cl) confirm the reliability of the structural models. Further atomic-scale evidence is provided by HR-TEM analysis of LSFSi-Cl, as shown in Fig. 2(b). Fast Fourier transform (FFT) patterns reveal spots corresponding to the (01$\bar{1}$), (1$\bar{1}$2), (10$\bar{1}$), and (1$\bar{1}$0) planes, with measured lattice spacings of 2.79, 1.61, 2.79, and 2.79 Å, respectively. The calculated lattice parameter of approximately 3.95 Å agrees well with the XRD refinement results and confirms that the codoped sample retains cubic symmetry. Together, these structural analyses demonstrate that both single doping and codoping preserve the perovskite framework while deliberately tuning the lattice parameters, thereby establishing a clear structural foundation for the subsequent investigations of electronic and electrochemical properties.

To understand how doping influences oxygen vacancy (Vo)

formation, which is a key factor governing proton conduction and oxygen reduction kinetics in H-SOFC cathodes [41], the O 1s XPS spectra of LSF, LSFSi, and LSFSi-Cl (Fig. 3(a)) were examined. The spectra were deconvoluted into contributions from lattice oxygen (O_{lat}), adsorbed oxygen species (O^{2-}/O^{-}), surface hydroxyl/carbonate groups (OH^{-}/CO_3^{2-}), and adsorbed water (O_H). The area ratio of (O^{2-}/O^{-}) to O_{lat}, often used as a qualitative indicator of oxygen vacancy concentration [42], decreases from 0.48 in LSF to 0.45 in LSFSi but rises markedly to 0.64 in LSFSi-Cl. This suggests that Si doping alone modestly suppresses Vo formation, while codoping with Cl substantially enhances it. To clarify the origin of this trend, DFT calculations were performed to determine the Vo formation energy at the most favorable site in each material. There are different possible configurations for the formation of Vo in LSF, LSFSi, and LSFSi-Cl (Fig. S2 in the ESM), and the most stable configuration is used for the Vo formation energy and bond lengths. As shown in Fig. 3(b), the Vo formation energy increases from 1.68 eV in LSF to 1.72 eV in LSFSi but drops sharply to 1.05 eV in LSFSi-Cl. These results align well with the XPS trend and indicate that Si raises the energy barrier for Vo creation, whereas Cl effectively lowers it. The substitution of Cl^{-} for O^{2-} introduces positively charged defect species $Cl_o^{\cdot}$ into the lattice. When coexisting with $Si_{Fe}^{\cdot}$, the strong local electrostatic repulsion and the structural distortion induced by the large ionic radius of Cl^{-} collectively lower the formation energy of oxygen vacancies. The lattice around $Cl_o^{\cdot}$ is more flexible and can better accommodate the strain associated with vacancy creation. Consequently, the charge compensation mechanism in the codoped system shifts toward the generation of a high concentration of oxygen vacancies, as confirmed by the reduction in Vo formation energy predicted by DFT and the increased Vo concentration evidenced by XPS. Differential charge density analysis (Fig. 3(c)) reveals the electronic redistribution underlying these energy changes. In LSFSi, pronounced charge depletion around Si and accumulation on neighboring oxygen atoms reflect strong electron transfer from Si^{4+} to oxygen ligands. This donor-like behavior strengthens both Si–O and nearby Fe–O bonds, rationalizing the increased Vo formation energy. In LSFSi-Cl, charge accumulation around two adjacent oxygen atoms weakens considerably. The lower electronegativity of Cl^{-} appears to relax the bonding network and facilitate charge compensation, thereby reducing the thermodynamic penalty for Vo formation [43]. Further insight comes from analyzing the local bond geometry in DFT-optimized structures. As illustrated in Fig. 3(d), in LSF, all Fe–O bonds are symmetric (1.96 Å). Si doping distorts this environment, elongating the Fe–O bond in an Fe–O–Si linkage to 2.08 Å while contracting the Si–O bond to 1.82 Å; a neighboring Fe–O bond in a standard Fe–O–Fe unit shortens to 1.92 Å, which is unfavorable for oxygen removal. Co-doping with Cl reconfigures the local structure, in which the Si–O bond shortens further to 1.69 Å and the associated Fe–O bond decreases to 1.89 Å. Importantly, an adjacent Fe–O bond in an Fe–O–Fe bridge elongates significantly to 2.34 Å. This locally weakened bond provides a preferential site for oxygen removal, directly explaining the drastically reduced Vo formation energy in LSFSi-Cl. Together, these results establish that while Si doping inhibits

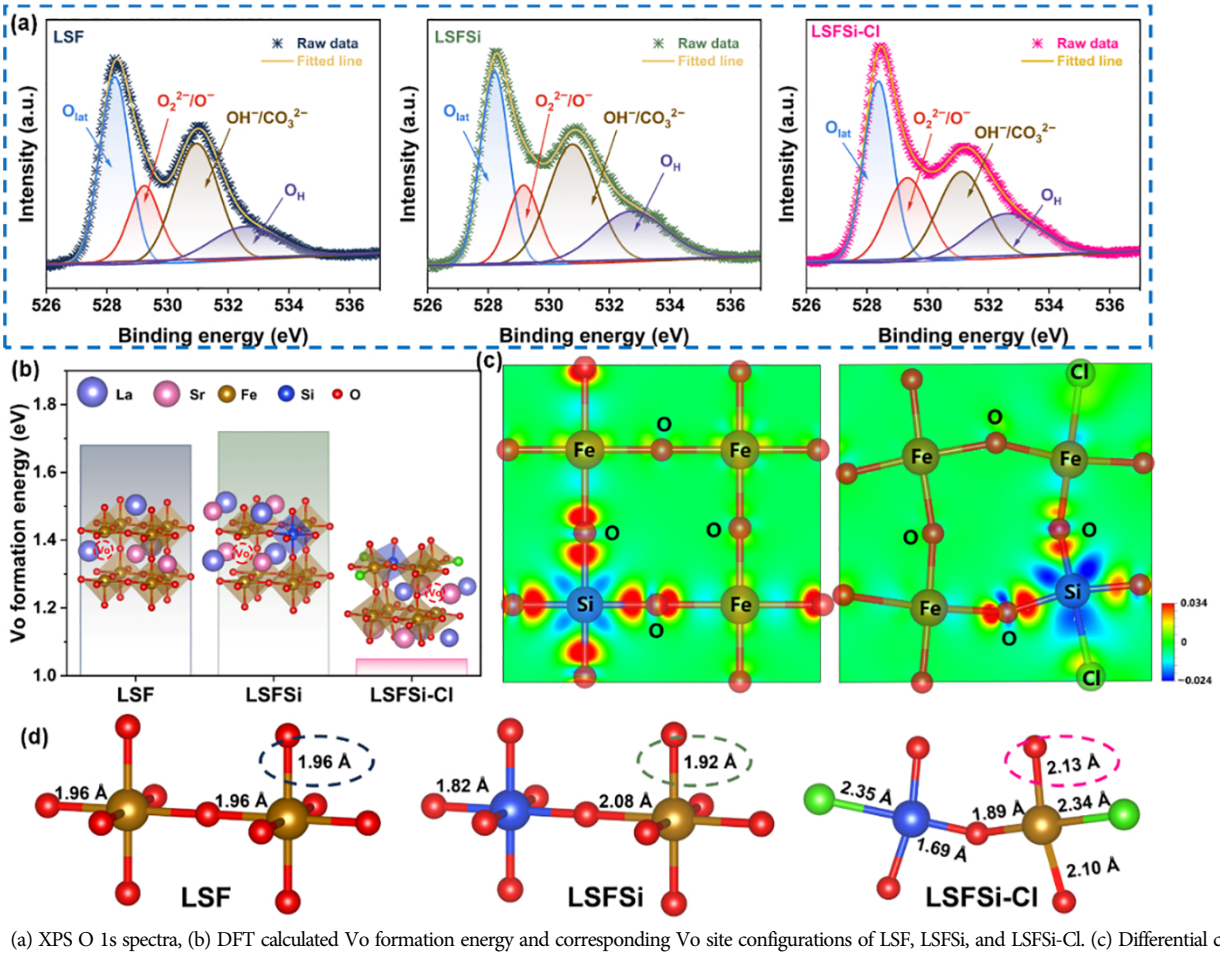

Fig. 3 (a) XPS O 1s spectra, (b) DFT calculated Vo formation energy and corresponding Vo site configurations of LSF, LSFSi, and LSFSi-Cl. (c) Differential charge density images of LSFSi and LSFSi-Cl. (d) Local bond geometry in DFT-optimized structures of LSF, LSFSi, and LSFSi-Cl.

Vo formation by strengthening metal–oxygen bonds, the simultaneous incorporation of Cl counteracts this effect by modulating electronic and structural properties, creating a more favorable local environment for vacancy generation. In addition, Cl doping is found to promote the electrical conductivity of LSF, whereas Si doping shows a clear suppressive effect (Fig. S3 in the ESM). Although this study selects Si contamination as a case study, it is found that Cl doping promotes charge redistribution and significantly reduces the energy barrier for Vo formation, which is a universal way to promote cathode performance. Therefore, the Cl-doping strategy may also be useful to compensate for other impurities.

The observed enhancement in the Vo concentration and the reduced formation energy for LSFSi-Cl prompted an investigation of their practical impact on oxygen transport kinetics. ECR measurements were therefore performed by abruptly changing the atmosphere from air to 50% O_2, monitoring the subsequent conductivity relaxation, which reflects the combined effects of bulk oxygen diffusion and surface exchange processes. As shown in Figs 4(a)–4(c), the normalized conductivity transients differ clearly among the three materials. Fitting these curves to the ECR model yields the oxygen diffusion coefficients (D_O) summarized in Fig. 4(d): 6.45×10^{-5} $cm^2\cdot s^{-1}$ for LSF, 3.61×10^{-5} $cm^2\cdot s^{-1}$ for LSFSi, and 9.12×10^{-5} $cm^2\cdot s^{-1}$ for LSFSi-Cl. The suppressed D_O in LSFSi corresponds to its higher oxygen vacancy formation energy, whereas the significantly increased value for LSFSi-Cl confirms improved bulk oxygen mobility. A similar trend can be seen in the surface exchange coefficients (K_O), which decrease from 7.92×10^{-4} cm s^{-1} (LSF) to 4.56×10^{-4} $cm\cdot s^{-1}$ (LSFSi) and then rise markedly to 2.23×10^{-3} $cm\cdot s^{-1}$ in LSFSi-Cl. This enhancement in surface kinetics can be linked to the expanded lattice free volume and favorable charge distribution in the co-doped material, which collectively facilitate oxygen dissociation and incorporation at the cathode surface.

Beyond oxygen transport, proton migration is also critical for the performance of H-SOFC cathodes [44–46]. To evaluate this property, analogous ECR measurements were performed by switching the atmosphere from dry air to humidified air at 600 °C, thereby isolating the contributions of proton diffusion and surface exchange [47]. The resulting relaxation profiles, shown in Figs. 5(a)–5(c), reveal distinct response times for each material. As shown in Fig. 5(d), fitting the data yields proton diffusion coefficients (D_H) of 7.33×10^{-5} $cm^2\cdot s^{-1}$ for LSF, 4.68×10^{-5} $cm^2\cdot s^{-1}$ for LSFSi, and 1.13×10^{-4} $cm^2\cdot s^{-1}$ for LSFSi-Cl. The proton surface exchange coefficients (K_H) follow a related trend, declining from 9.25×10^{-4} $cm\cdot s^{-1}$ in LSF to 5.67×10^{-4} $cm\cdot s^{-1}$ in LSFSi, which reflects the disruptive influence of Si doping on water adsorption. In contrast, K_H rises notably to 2.83×10^{-3} $cm\cdot s^{-1}$ for the co-doped LSFSi-Cl. This enhancement suggests that the charge delocalization induced by Cl promotes the dissociative incorporation of water at the surface, thereby facilitating proton uptake and transport [48].

The characterization results indicate that Si doping in LSF leads to lattice contraction, suppresses oxygen vacancy concentration, and raises the oxygen vacancy formation energy, thereby impairing both oxygen and proton transport kinetics. In contrast, codoping with Cl counteracts these detrimental effects through electronic charge delocalization and bond modulation, which promote vacancy formation, lower the associated energy barrier, and significantly enhance bulk diffusion and surface exchange processes. Based on these improvements, LSFSi-Cl is expected to deliver superior performance in an operating H-SOFC compared to both LSF and LSFSi. To verify this prediction, single-cell tests were conducted using anode-supported configurations with a

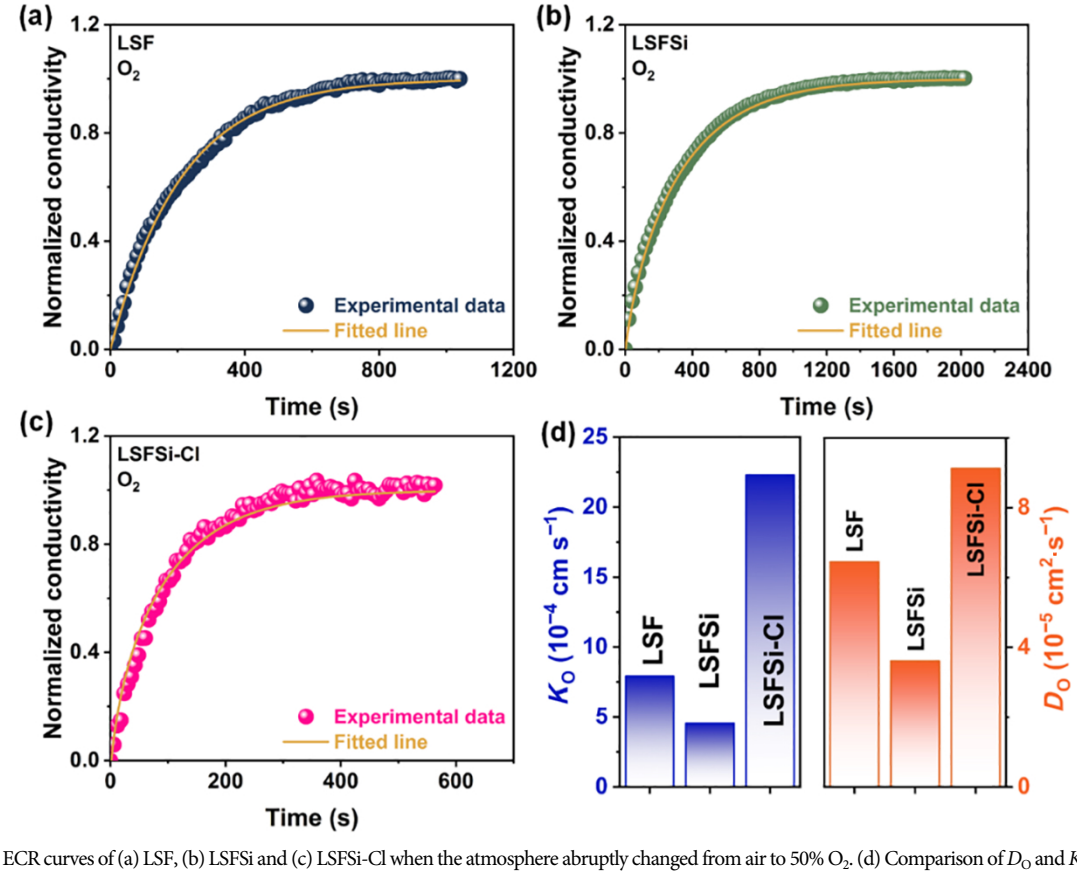

Fig. 4 ECR curves of (a) LSF, (b) LSFSi and (c) LSFSi-Cl when the atmosphere abruptly changed from air to 50% O_2. (d) Comparison of D_O and K_O values.

BCZY electrolyte. The chemical compatibility between the LSFSi-Cl and BCZY electrolytes was examined (Fig. S4 in the ESM), showing that no evident reaction can be seen between LSFSi-Cl and BCZY even after co-firing at 900 °C, which indicates good chemical compatibility between these two oxides. The *I*–*V* and power density curves at 600–700 °C are shown in Figs. 6(a)–6(c). The peak power densities (PPDs) in Fig. 6(d) show that the LSF cathode reaches 688, 521, and 383 mW·cm^{-2} at 700, 650, and 600 °C, respectively. With Si doping (LSFSi), the PPDs decline to 563, 409, and 275 mW·cm^{-2}, consistent with the detrimental

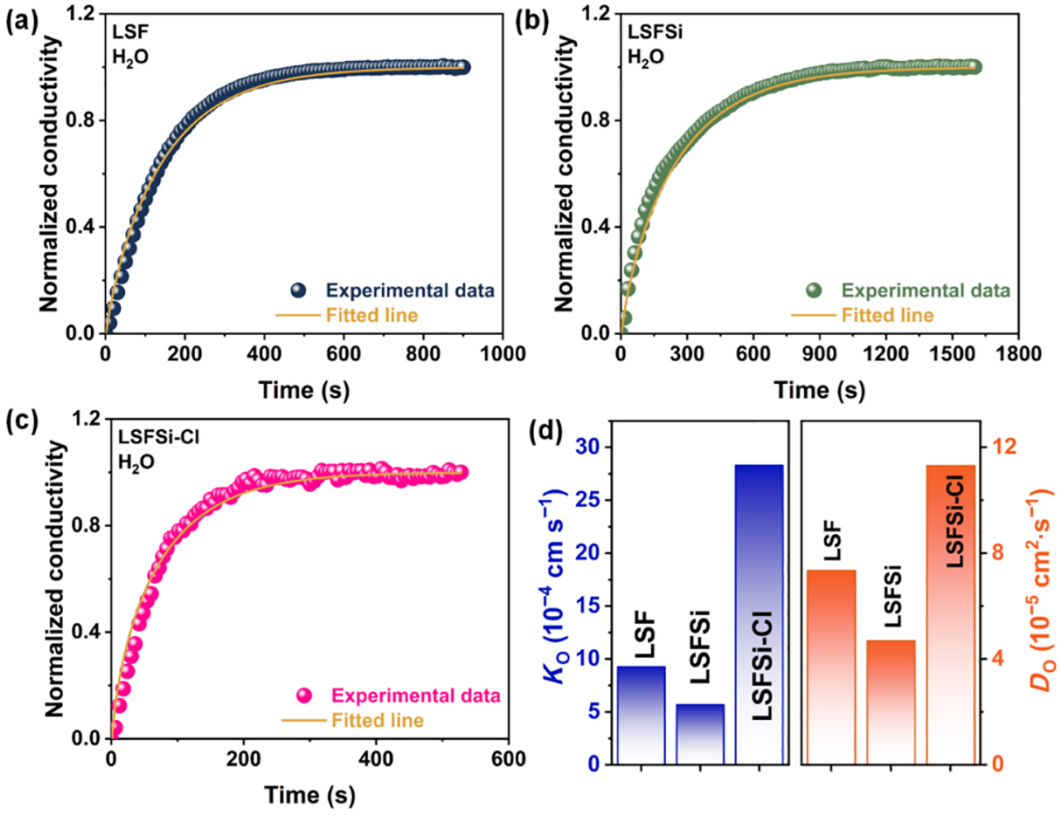

Fig. 5 ECR curves of (a) LSF, (b) LSFSi and (c) LSFSi-Cl when the atmosphere abruptly changed from dry to humidified air. (d) Comparison of D_H and K_H values.

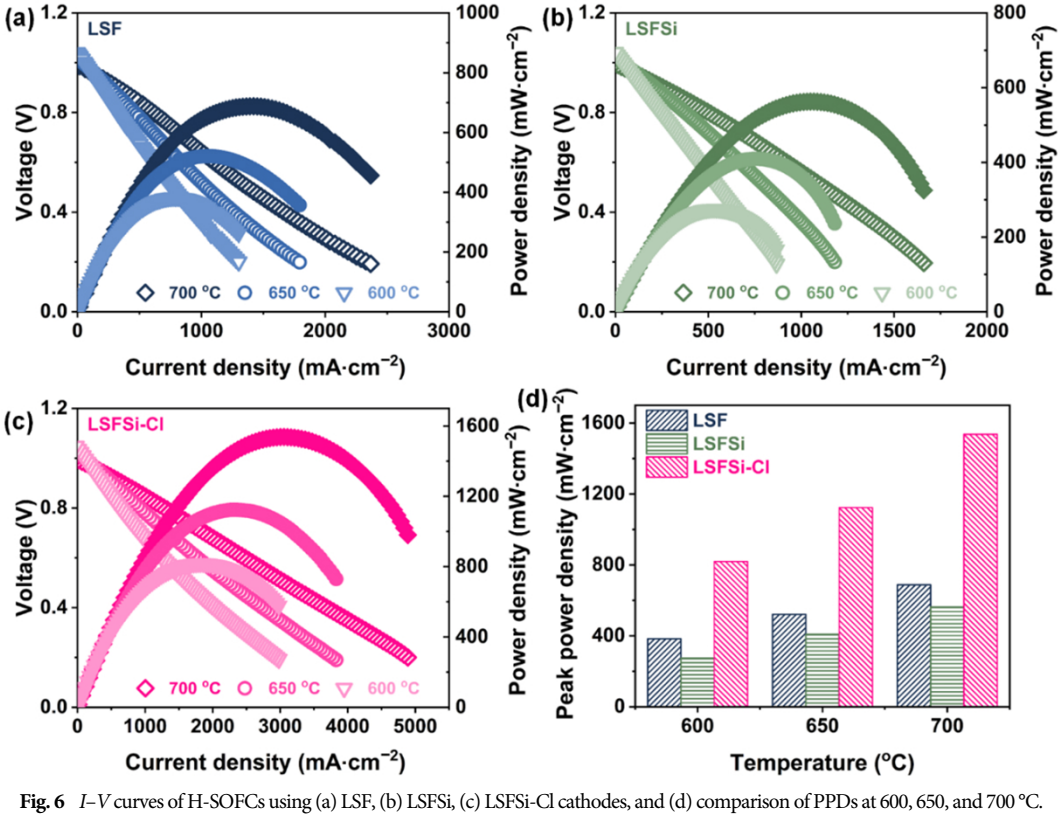

Fig. 6 *I*–*V* curves of H-SOFCs using (a) LSF, (b) LSFSi, (c) LSFSi-Cl cathodes, and (d) comparison of PPDs at 600, 650, and 700 °C.

influence of Si on transport properties. Remarkably, the LSFSi-Cl cathode exhibits a substantial recovery, achieving PPDs of 1537, 1123, and 819 mW·cm^{-2} at the same temperatures. These results clearly demonstrate that Cl codoping not only mitigates the poisoning effect of Si but also elevates the cell performance well beyond that of the pristine LSF. It is noted that although the pristine LSF is a well-known cathode for SOFCs, its performance of H-SOFCs is not very satisfactory [34]. Tailoring LSF cathodes with improved performance has been achieved in the past few years [49,50]. Even compared with these tailored LSF cathodes, the PPD of the cell with the LSFSi-Cl cathode still shows advantages. However, it should be admitted that the performance of the LSFSi-Cl cathode is inferior to that of some recently developed high-performing cathodes for H-SOFCs [18,19,41], which is probably due to its Ba and Co-free composition. Ba can usually improve the hydration of the material, while the incorporation of Co can lead to an increase in catalytic activity [51,52], which might be a further strategy for improving the performance of LSFSi-Cl cathodes.

Post-test cross-sectional SEM images of the single cells employing LSF, LSFSi, and LSFSi-Cl cathodes are shown in Fig. 7. The three cells exhibit comparable microstructures, each featuring a dense electrolyte layer that adheres well to both the porous cathode and anode. This structural consistency confirms that the observed differences in electrochemical performance do not stem from variations in electrode morphology or interfacial integrity. Given that the anode composition and cell fabrication were identical across all samples, the substantial divergence in fuel cell output can be directly attributed to the intrinsic properties of the cathode materials themselves.

Electrochemical impedance spectroscopy (EIS) was conducted under open-circuit conditions with a frequency range from 1 MHz to 0.1 Hz to further elucidate the electrochemical behavior of the cathodes. The resulting Nyquist plots (Figs. 8(a)–8(c)) distinguish the ohmic resistance (R_o), polarization resistance (R_p), and total cell resistance (R_{tot}). At 700 °C, R_o values are similar across the three cells, which are 0.106, 0.111, and 0.102 Ω·cm^2 for LSF, LSFSi, and LSFSi-Cl, respectively, consistent with their comparable electrolyte thickness and microstructure. In contrast, R_p varied significantly, increasing from 0.122 Ω·cm^2 for LSF to 0.158 Ω·cm^2 for LSFSi but dropping sharply to 0.042 Ω·cm^2 for LSFSi-Cl. This trend in polarization resistance directly accounts for the differences in total resistance and aligns with the observed peak power densities. The kinetic origin of this enhancement is further clarified by the activation energy (E_a) derived from Arrhenius fitting of R_p. As shown in Fig. 8(d), LSFSi-Cl exhibits the lowest E_a (0.61 eV), substantially smaller than that of LSF (0.88 eV) and LSFSi (0.93 eV). This reduced energy barrier for oxygen reduction is consistent with the DFT-calculated lowering of the vacancy formation energy, confirming that the synergistic interaction between Si and Cl not only promotes vacancy generation but also accelerates the overall cathode reaction kinetics.

One may wonder whether the increase or decrease in the Cl-doping concentration in the oxide would further enhance the fuel cell performance. Therefore, different Cl concentration-doped

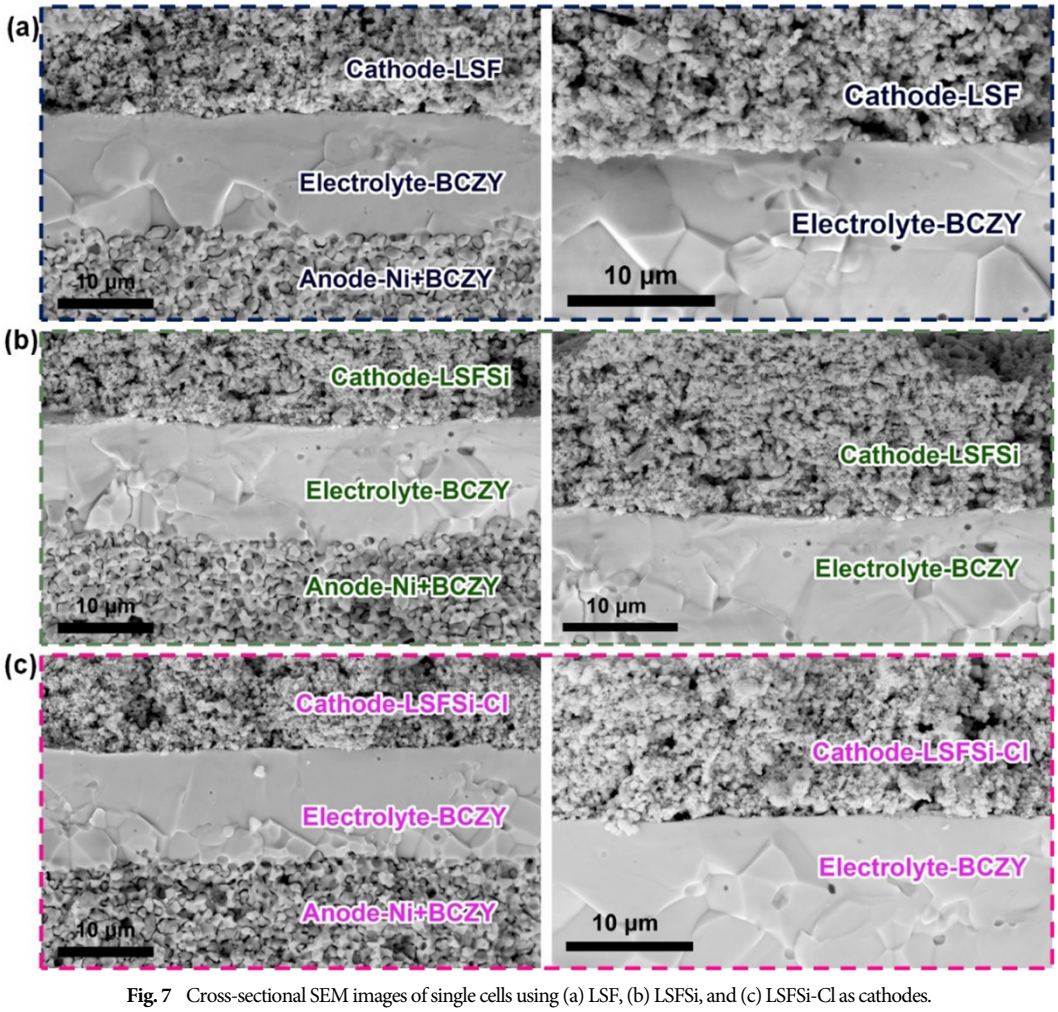

Fig. 7 Cross-sectional SEM images of single cells using (a) LSF, (b) LSFSi, and (c) LSFSi-Cl as cathodes.

清華大学出版社 Tsinghua University Press | SciOpen

oxides, including $La_{0.5}Sr_{0.5}Fe_{0.95}Si_{0.05}Cl_{0.05}O_{2.95-\delta}$ (LSFSi-Cl0.05), $La_{0.5}Sr_{0.5}Fe_{0.95}Si_{0.05}Cl_{0.2}O_{2.8-\delta}$ (LSFSi-Cl0.2) and $La_{0.5}Sr_{0.5}Fe_{0.95}Si_{0.05}Cl_{0.4}O_{2.6-\delta}$ (LSFSi-Cl0.4), were prepared. As shown in Fig. S5 in the ESM, when the doping concentration is 0.05, 0.1, and 0.2, the materials exhibit pure phases. When the doping concentration reaches 0.4, distinct peak splitting is observed in the XRD patterns, indicating the onset of phase separation and the loss of a single-phase structure. Therefore, the following work is focused on pure phase materials. The performance of H-SOFCs using LSFSi-Cl0.05, LSFSi-Cl and LSFSi-Cl0.2 cathodes is evaluated. The

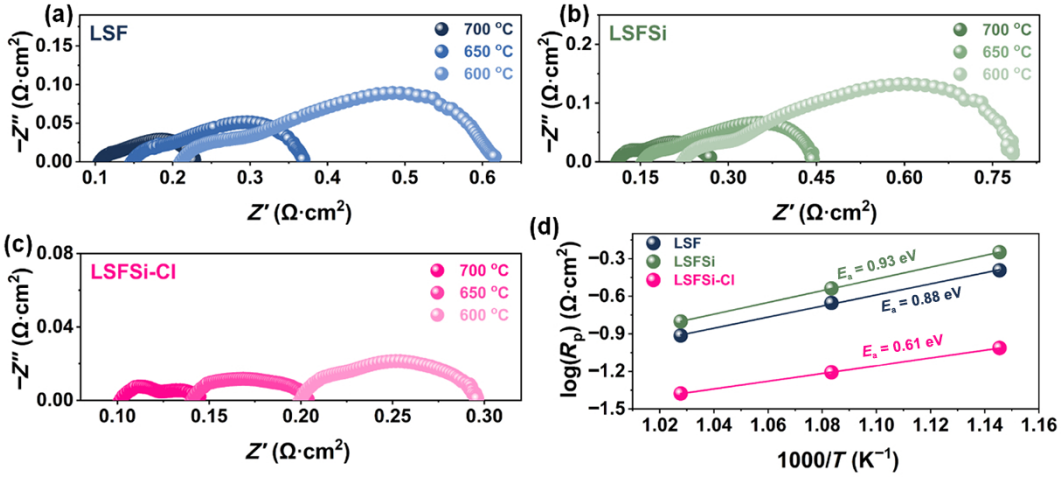

Fig. 8 EIS plots of (a) LSF, (b) LSFSi, (c) LSFSI-Cl cells, and (d) Arrhenius fitting of R_p.

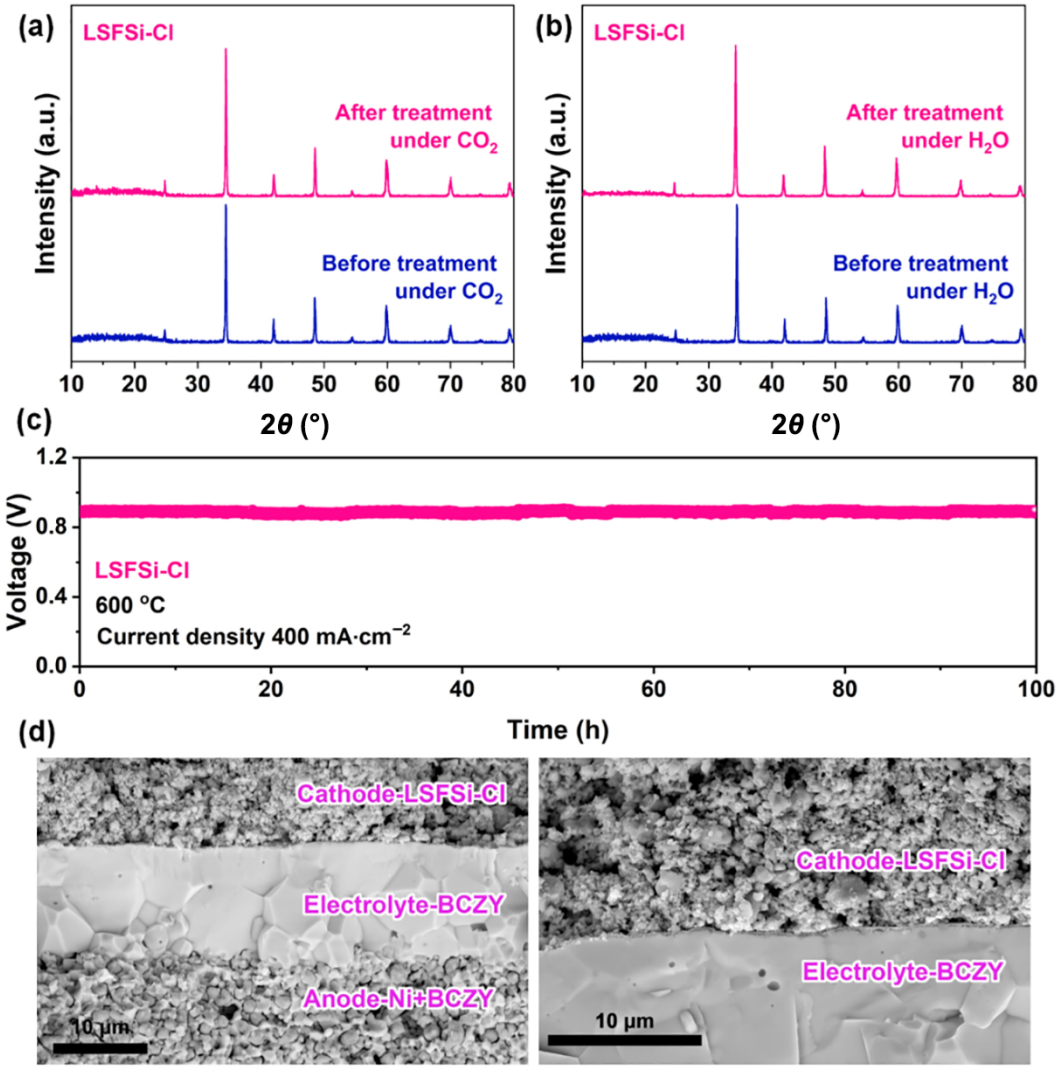

Fig. 9 XRD patterns of LSFSi-Cl before and after exposure to (a) 20% CO_2 atmosphere and (b) 30% H_2O air at 600 °C for 10 h. (c) Long-term stability test of single cells using the LSFSi-Cl cathode. (d) Cross-sectional SEM images of single cells after the long-term stability test.

PPD of the cell with the LSFSi-Cl0.05 cathode is 422, 611, and 847 mW cm^{-2} at 600, 650, and 700 °C, respectively, and the PPD of the cell using the LSFSi-Cl0.2 cathode is 524, 857, and 1208 mW·cm^{-2} at 600, 650, and 700 °C, respectively (Figs. S6(a) and S6(b) in the ESM). Both cells show lower performance than that of the cell using the LSFSi-Cl cathode. By analyzing their resistance (Figs. S6(c) and S6(d) in the ESM), it is found that the R_p values of the LSFSi-Cl0.05 and LSFSi-Cl0.2 cells are 0.098 and 0.063 Ω·cm^2 at 700 °C, respectively, which are higher than that for the LSFSi-Cl cell. All this evidence indicates that a Cl-doping concentration of 0.1 is the optimal amount, which enhances the cathode catalytic activity and fuel cell performance.

Given the exceptional electrochemical performance of LSFSi-Cl, particularly its low polarization resistance and high-power density at intermediate temperatures, durability is a critical requirement for practical H-SOFCs where cathodes are exposed to humid or CO_2-containing atmospheres. Chemical stability was first assessed by exposing LSFSi-Cl powder to atmospheres containing 20% CO_2 or 30% H_2O at 600 °C for 10 h. As shown in Figs. 9(a) and 9(b), the XRD patterns before and after exposure retain the pristine perovskite structure without any detectable secondary phases, confirming the material's robustness under these aggressive conditions. Under real working conditions, the CO_2 content in the air is only 0.03%, and the H_2O content in the humidified H_2 (the fuel) is only 3%, which are much lower than those used in the chemical stability test. The material can show sufficient stability even under more severe conditions, suggesting its good chemical stability in fuel cell working conditions. Operational stability was further examined in a single cell operating at 600 °C under a constant current density of 400 mA·cm^{-2}. The cell voltage remained nearly unchanged over 100 h (Fig. 9(c)), demonstrating excellent performance retention. The voltage of the cell before and after the long-term test is 0.892 and 0.888 V, respectively, indicating a degradation rate of 0.45% per 100 h. The posttest cross-sectional SEM images in Fig. 9(d) revealed that the cathode-electrolyte interface remained dense, adherent, and free of delamination or microcracks. Together, these results indicate that LSFSi-Cl not only delivers superior activity but also possesses the chemical and mechanical durability necessary for long-term operation.

4 Conclusions

In summary, this work demonstrates that anion regulation via chloride doping offers an effective strategy to counteract the detrimental effects of silicon impurities in perovskite cathodes for H-SOFCs. While silicon doping alone in $La_{0.5}Sr_{0.5}FeO_3$ increases the formation energy of oxygen vacancies, contracts the lattice, and consequently degrades oxygen and proton transport, codoping with chloride systematically reverses these negative trends. DFT calculations reveal that Cl incorporation facilitates charge redistribution and significantly lowers the energy barrier for vacancy formation while expanding the lattice volume and weakening specific metal-oxygen bonds. These changes enhance both bulk diffusion and surface exchange kinetics. As a result, the Si-Cl co-doped cathode achieves a peak power density of 1537 mW·cm^{-2} at 700 °C, along with excellent stability under CO_2 and moisture, and prolonged operation. These findings illustrate that anion engineering can remediate cation-impurity poisoning, providing a practical design pathway to develop cost-effective, durable, and impurity-tolerant cathodes for H-SOFCs.

Acknowledgements

This work was supported by the National Natural Science Foundation of China (Grant Nos. 52302263 and 52572230).

Author contributions

Wenhui Song: investigation, formal analysis, writing – original draft. Xianchen Dong: investigation, validation. Yanru Yin: investigation, software. Shoufu Yu: validation. Yueyuan Gu: conceptualization, formal analysis, writing – review & editing. Lei Bi: writing – review & editing, project administration.

Availability of data and materials

The data that support the findings of this study are available from the corresponding author upon reasonable request.

Competing interests

The authors have no competing interests to declare that are relevant to the content of this article. The author Lei Bi is the Associate Editor of this journal.

Electronic Supplementary Material

Supplementary material is available in the online version of this article at https://doi.org/10.26599/JAC.2026.9221262.

References

[1] Zhang Y, Chen B, Guan DQ, *et al.* Thermal-expansion offset for high-performance fuel cell cathodes. *Nature* 2021, **591**: 246–251.
[2] Liu F, Deng H, Wang ZX, *et al.* Synergistic effects of *in-situ* exsolved Ni–Ru bimetallic catalyst on high-performance and durable direct-methane solid oxide fuel cells. *J Am Chem Soc* 2024, **146**: 4704–4715.
[3] Zhang Y, Knibbe R, Sunarso J, *et al.* Recent progress on advanced materials for solid-oxide fuel cells operating below 500 °C. *Adv Mater* 2017, **29**: 1700132.
[4] Kilner JA, Burriel M. Materials for intermediate-temperature solid-oxide fuel cells. *Annu Rev Mater Res* 2014, **44**: 365–393.
[5] Wang Z, Yuan MK, Gao JT, *et al.* Effective suppression of surface cation segregations on double perovskite oxides through entropy engineering. *J Rare Earths* 2025, **43**: 345–353.
[6] Wachsman ED, Lee KT. Lowering the temperature of solid oxide fuel cells. *Science* 2011, **334**: 935–939.
[7] Chen M, Chen DC, Wang K, *et al.* Densification and electrical conducting behavior of $BaZr_{0.9}Y_{0.1}O_{3-\delta}$ proton conducting ceramics with NiO additive. *J Alloys Compd* 2019, **781**: 857–865.
[8] Zhou XK, Shi BC, Yu XL, *et al.* A novel protonic ceramic fuel cell with $SrSn_{0.8}Sc_{0.2}O_{3-\delta}$ electrolyte. *J Eur Ceram Soc* 2024, **44**: 5814–5822.
[9] Zvonareva I, Fu XZ, Medvedev D, *et al.* Electrochemistry and energy conversion features of protonic ceramic cells with mixed ionic-electronic electrolytes. *Energy Environ Sci* 2022, **15**: 439–465.
[10] Chen ML, Zhao K, Li J, *et al.* Separation of hydrogen isotopes using a protonic ceramic fuel cell. *J Mater Chem A* 2025, **13**: 7687–7691.
[11] Ge L, Jiao JH, zhu ZC, *et al.* A facile method to fabricate proton-conducting $BaZr_{0.85}Y_{0.15}O_3$ electrolyte with a large grain size and high conductivity. *Ceram Int* 2019, **45**: 24946–24952.
[12] Li XY, Chen ZM, Huan DM, *et al.* Highly active cathode achieved by constructing surface proton acid sites through electronic regulation of heteroatoms. *ACS Mater Lett* 2023, **5**: 2896–2905.
[13] Zhou R, Yin YR, Dai HL, *et al.* Attempted preparation of $La_{0.5}Ba_{0.5}MnO_{3-\delta}$ leading to an *in-situ* formation of manganate nanocomposites as a cathode for proton-conducting solid oxide fuel cells. *J Adv Ceram* 2023, **12**: 1189–1200.
[14] Liu CZ, Liu B, Li ZF, *et al.* Interface-engineering to boost the performance and durability of nickel-metal-supported reversible proton ceramic cells for power generation and hydrogen production. *J Adv Ceram* 2025, **14**: 9221115.
[15] Yin YR, Liu B, Yan D, *et al.* Balancing intrinsic properties of cathode materials allows high performance for protonic ceramic fuel cells. *SusMat* 2024, **4**: 262.

[16] Gao JT, Liu YY, Gao Y, *et al.* Cobalt-free fluorine doped $Bi_{0.7}Sr_{0.3}FeO_3$ oxides for energetic cathodes of low-temperature solid oxide fuel cells. *Chem Eng J* 2023, **452**: 139584.
[17] Wang N, Yuan BY, Zheng FY, *et al.* Machine-learning assisted screening proton conducting Co/Fe based oxide for the air electrode of protonic solid oxide cell. *Adv Funct Mater* 2024, **34**: 2309855.
[18] Wang Z, Wang YH, Wang J, *et al.* Rational design of perovskite ferrites as high-performance proton-conducting fuel cell cathodes. *Nat Catal* 2022, **5**: 777–787.
[19] Yin YR, Huang HF, Boulfrad S, *et al.* Breaking the limits of Ruddlesden–Popper cathodes to achieve a game-changer for proton-conducting solid oxide fuel cells. *Energy Environ Sci* 2025, **18**: 8130–8141.
[20] Gao JT, Wei ZY, Yuan MK, *et al.* Boosting oxygen reduction activity and CO_2 resistance on bismuth ferrite-based perovskite cathode for low-temperature solid oxide fuel cells below 600 °C. *J Energy Chem* 2024, **90**: 600–609.
[21] Wang Z, Li JW, Yuan MK, *et al.* A medium-entropy engineered double perovskite oxide for efficient and CO_2-tolerant cathode of solid oxide fuel cells. *Sustain Mater Technol* 2024, **40**: 00969.
[22] Wang CC, Darvish S, Chen KF, *et al.* Combined Cr and S poisoning of $La_{0.8}Sr_{0.2}MnO_{3-\delta}$ (LSM) cathode of solid oxide fuel cells. *Electrochim Acta* 2019, **312**: 202–212.
[23] Schulze-Küppers F, Duburg JC, Deibert W, *et al.* Interaction between proton conducting $BaCe_{0.2}Zr_{0.7}Y_{0.1}O_3$ electrolyte and structural ceramics during sintering. *J Eur Ceram Soc* 2024, **44**: 2762–2769.
[24] Gao Y, Ling YH, Yuan MK, *et al.* Praseodymium Double-site occupancy to enhance the activity and impurity tolerance of $SrCo_{0.9}Ta_{0.1}O_{3-\delta}$ cathode for solid oxide fuel cells. *Fuel* 2025, **393**: 135033.
[25] Yang YG, Ren HS, Xie TY, *et al.* The modification and strengthening dual functionality of rare-earth oxide in La_2O_3–BaO–SiO_2 glass for high temperature sealing application. *J Alloys Compd* 2023, **950**: 169892.
[26] Liu Y, Zhu XF, Li MR, *et al.* Degradation and stabilization of perovskite membranes containing silicon impurity at low temperature. *J Membr Sci* 2015, **492**: 173–180.
[27] Yin YR, Zhang SQ, Wang A, *et al.* Rational design of $PrBaFe_2O_{6-\delta}$-based cathodes for protonic ceramic fuel cells. *J Adv Ceram* 2024, **13**: 1600–1610.
[28] Wang YJ, Jiang SS, Tu JJ, *et al.* Enhanced oxygen reduction reaction activity of Na^+ and Ce^{4+} co-doped $SrCoO_{3-\delta}$ cathode for protonic ceramic fuel cells. *Mater Sci Eng B* 2025, **318**: 118264.
[29] Yuan BY, Wang N, Tang CM, *et al.* Advances and challenges in high-performance cathodes for protonic solid oxide fuel cells and machine learning-guided perspectives. *Nano Energy* 2024, **122**: 109306.
[30] He F, Zhou YC, Hu T, *et al.* An efficient high-entropy perovskite-type air electrode for reversible oxygen reduction and water splitting in protonic ceramic cells. *Adv Mater* 2023, **35**: 2209469.
[31] Xu Y, Huang YL, Guo YM, *et al.* Engineering anion defect in perovskite oxyfluoride cathodes enables proton involved oxygen reduction reaction for protonic ceramic fuel cells. *Sep Purif Technol* 2022, **290**: 120844.
[32] Li X, Xia T, Dong ZW, *et al.* Unveiling positive impacts of fluorine anion doping on extraordinary catalytic activity of bifunctional-layered double perovskite electrodes for solid oxide fuel cells and electrolysis cells. *Mater Today Chem* 2023, **29**: 101469.
[33] Dong XC, Yu SF, Gu YY, *et al.* Tailoring $SrFeO_3$ cathode with Ta and F allows high performance for proton-conducting solid oxide fuel cells. *Sustain Mater Techno* 2024, **41**: 01104.
[34] Yamaura H, Ikuta T, Yahiro H, *et al.* Cathodic polarization of strontium-doped lanthanum ferrite in proton-conducting solid oxide fuel cell. *Solid State Ion* 2005, **176**: 269–274.
[35] Yin YR, Xiao DD, Wu S, *et al.* A real proton-conductive, robust, and cobalt-free cathode for proton-conducting solid oxide fuel cells with exceptional performance. *SusMat* 2023, **3**: 697–708.
[36] Dai HL, Du HZ, Boulfrad S, *et al.* Manipulating Nb-doped $SrFeO_{3-\delta}$ with excellent performance for proton-conducting solid oxide fuel cells. *J Adv Ceram* 2024, **13**: 579–589.
[37] Kresse G, Furthmüller J. Efficient iterative schemes for *ab initio* total-energy calculations using a plane-wave basis set. *Phys Rev B* 1996, **54**: 11169–11186.
[38] Kresse G, Joubert D. From ultrasoft pseudopotentials to the projector augmented-wave method. *Phys Rev B* 1999, **59**: 1758–1775.
[39] Kohn W, Sham LJ. Self-consistent equations including exchange and correlation effects. *Phys Rev* 1965, **140**: A1133–A1138.
[40] Payne MC, Teter MP, Allan DC, *et al.* Iterative minimization techniques for *ab initio* total-energy calculations: Molecular dynamics and conjugate gradients. *Rev Mod Phys* 1992, **64**: 1045–1097.
[41] Yin YR, Zhou YB, Gu YY, *et al.* Successful preparation of $BaCo_{0.5}Fe_{0.5}O_{3-\delta}$ cathode oxide by rapidly cooling allowing for high-performance proton-conducting solid oxide fuel cells. *J Adv Ceram* 2023, **12**: 587–597.
[42] Zhang XH, Pei CL, Chang X, *et al.* FeO_6 octahedral distortion activates lattice oxygen in perovskite ferrite for methane partial oxidation coupled with CO_2 splitting. *J Am Chem Soc* 2020, **142**: 11540–11549.
[43] Yang S, Wang LL, Yu SF, *et al.* Achieving balanced electrochemical performance and durability in H-SOFCs via Ga-doping in $La_{0.5}Sr_{0.5}FeO_3$ cathodes. *Mater Sci Eng B* 2025, **322**: 118674.
[44] Xu YS, Xu K, Zhu F, *et al.* A low-lewis-acid-strength cation Cs^+-doped double perovskite for fast and durable oxygen reduction/evolutions on protonic ceramic cells. *ACS Energy Lett* 2023, **8**: 4145–4155.
[45] Gu YH, Chen ZY, Wang ZC, *et al.* Avoiding undesirable cathode/electrolyte interfacial reactions for proton-conducting solid oxide fuel cells by Joule heating. *J Adv Ceram* 2025, **14**: 9221040.
[46] Ma ZL, Ye QR, Zhang BK, *et al.* A highly efficient and robust bifunctional perovskite-type air electrode with triple-conducting behavior for low-temperature solid oxide fuel cells. *Adv Funct Mater* 2022, **32**: 2209054.
[47] Ren RZ, Wang ZH, Meng XG, *et al.* Tailoring the oxygen vacancy to achieve fast intrinsic proton transport in a perovskite cathode for protonic ceramic fuel cells. *ACS Appl Energ Mater* 2020, **3**: 4914–4922.
[48] Ding HP, Wu W, Jiang C, *et al.* Self-sustainable protonic ceramic electrochemical cells using a triple conducting electrode for hydrogen and power production. *Nat Commun* 2020, **11**: 1907.
[49] He SC, Dai HL, Bi L. A highly efficient Sb-doped $La_{0.5}Sr_{0.5}FeO_{3-\delta}$ cathode for protonic ceramic fuel cells. *Ceram Int* 2024, **50**: 1284–1292.
[50] Xu X, Xu YS, Ma JM, *et al.* Tailoring electronic structure of perovskite cathode for proton-conducting solid oxide fuel cells with high performance. *J Power Sources* 2021, **489**: 229486.
[51] Dai HL, Bi L. High-entropy cathodes for proton-conducting solid oxide fuel cells: A promising yet uncharted frontier. *SusMat* 2025: 70054.
[52] Gu YY, Shi J, Nematov D, *et al.* A brief review of high-entropy oxides in solid oxide fuel cell applications. *Mater Sci Eng B* 2026, **327**: 119260.